INTERNATIONAL JOURNAL OF HYDROGEN ENERGY 45 (2020) 1901–1910

Available online at www.sciencedirect.com

ScienceDirect

journal homepage: www.elsevier.com/locate/he

Stacked Co_6W_6C nanocrystals anchored on N-doping carbon nanofibers with excellent electrocatalytic performance for HER in wide-range pH

*Yini Fang, Ting Zhang, Yudong Wu, Yuanjian Liu, Jibiao Guan, Xiangheng Du, Lina Wang, Ming Zhang**

School of Materials Science and Engineering, Zhejiang Sci-Tech University, Hangzhou, 310018, PR China

HIGHLIGHTS

- Co_6W_6C–N@CNFs expose numerous active sites for HER with the ultrathin size.
- The synergetic effect in Co_6W_6C–N@CNFs boosts the catalystic performance.
- The modification of N-doping optimizes the adsorption energy of Co_6W_6C–N@CNFs surface.
- Co_6W_6C–N@CNFs exhibit outstanding HER properties both in acidic and base.
- Exceeding carbon provides protection with Co_6W_6C to achieve durable stability.

GRAPHICAL ABSTRACT

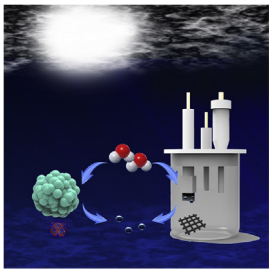

ARTICLE INFO

Article history:
Received 8 August 2019
Received in revised form
6 November 2019
Accepted 15 November 2019
Available online 19 December 2019

ABSTRACT

High purity H_2 formed by electrochemical water splitting is profound potential green energy. Exploiting advanced electrocatalysts for hydrogen evolution reaction (HER) in both acidic and base environment is of critical significance. Herein, we report a novel hybrid comprising stacked cobalt tungsten carbides nanocrystals on N-doping carbon matrix (Co_6W_6C–N@CNFs) as a superb HER catalyst over the entire pH range via facile electrospinning and CVD method. On account of its ultrathin size and the strong synergetic interaction between bimetals, coupled with the superior conductivity of N-doping CNFs, Co_6W_6C–N@CNFs presents superior catalytic properties, with low overpotentials of 86 and

* *Corresponding author.*
E-mail addresses: 2016339901214@mails.zstu.edu.cn (Y. Fang), ddtongxue@163.com (T. Zhang), yudongwu518@gmail.com (Y. Wu), 2018339910017@mails.zstu.edu.cn (Y. Liu), guanjibiao@hotmail.com (J. Guan), 1852897024@qq.com (X. Du), lnwang@zstu.edu.cn (L. Wang), zhangming@zstu.edu.cn (M. Zhang).
https://doi.org/10.1016/j.ijhydene.2019.11.123

Keywords:
Co_6W_6C
TMCs
All-pH values
Hydrogen evolution reaction

116 mV at η_{10} and small Tafel slopes of 85 and 101 mV dec^{-1} in acidic and alkali, respectively, as well as outstanding long-term stability, rivalling its potential to be used intensively in water electrolysis technologies.

Introduction

The environmental pollutions and fossil fuel-starved future are main pressing issues to 21st century. Hydrogen energy has been recognized as promising alternative to supersede conventional fossil fuel. Among plentiful methods for large-scale hydrogen production [1–4], water electrolysis with zero emission and genuine purity of H_2 has captured intense attention [5]. In order to improve the efficiency of water splitting, great effort has been devoted, for instance, exploring reaction kinetic [6,7], optimizing electrolyze [8] and most attractively, designing and synthesizing excellent nanostructured electrocatalysts. To date, the main HER electrocatalysts are aimed to acidic condition, due to faster reaction kinetics than that in base [9], nonetheless, it is become increasingly arduous to ignore pH-universal HER catalysts to meet the demands. Owing to the all-pH efficiency and durable HER catalytic performance [10], Pt-based materials have remained the commercial benchmark catalysts by far, yet the dearth and valuableness of Pt impede their wide application. Thence, great endeavors have been focused on precious-metal-free electrocatalysts for HER in all-pH values, like metal alloys [11,12], oxides [13], nitrides [14], nanocarbon-based materials [15–17] and transition metal compounds (TMCs [18,19], TMDs [20–23] and TMPs [17,21,24,25]) to achieve small overpotentials and fast reaction kinetic.

As an ideal catalyst, it demands both the intrinsic catalytic activities and high efficiency of charge transfer. By known the superior conductivity of graphene [26], carbon-based materials have been widely applied as reactors for electrocatalysts [27–29]. In addition to that, ascribing to the different electronegativity between C and N [30–32], N-doping carbon materials have been intensively explored [17,25,33] in electrochemistry field. The excellent conductivity, high specific surface area, as well as the tunable surface properties of carbon nanofibers, and the modification behavior of N atoms which can be used to tune the electrical properties of CNFs and create highly localized states near the Fermi level, contributing to favorable adsorption [34,35] makes N-doping carbon materials efficiently promoting the charge transfer process during HER [36,37]. Moreover, carbon layers can protect metal catalysts simultaneously from corrosion and enhance the stability in both acidic and alkaline environment [38].

Otherwise, transition metals (TMs) possess excellent electrochemical performance due to their exceptional natural 3d orbit electron configuration, which can provide abundant active sites to adsorb H^* [39]. Among TMs, Cobalt-based materials with their stunning catalytic activities [40,41] are one of the most widely used groups for HER. Moreover, tungsten was confirmed its Pt-like catalytic behaviors half a century ago [42], making it emerged as preferred catalysts for HER. Yet, monoatomic catalysts are liable to be corroded by solution which gives rise to reduce their instinct catalytically properties [9]. Over the years, bimetal carbides have increasingly been recognized by prominent electrocatalytical activities, not only because they could accelerate the graphitization of the carbon species to enhance the resistance to electrochemical oxidation [36], but also for their unique synergetic effects between two metals that reaps huge fruits to the charge transfer process [43]. Researchers therefore, paid a great deal of effort to investigate transtion metal carbides (TMCs), such as Ni–Fe@C [44], Co–Cu@C [36], Ni–Mo/C [45], Ni–W@C [46] (Table S1), but the exploration of Co–W–C is limited. Traditionally, TMCs are synthesized via liquid metal solvent based co-segregation strategy [42], $NaBH_4$ reduction [47], impregnation method [19] and in-site solid state reaction [48]. However, these approaches fail to precise control of catalyst particle sizes, and powder outcomes need to be further processed during electrochemical test stage, as well as the weak binding between catalyst and substrate obstacle their universal application.

In this work, we proposed an environmentally-friendly electrospun method to achieve TMCs nanoparticles anchored closely in N-doping carbon nanofibers with PAN as the precursor of N and C with no more excrescent carbon additions, taking advantage of the nano-confinement effect of electrospinning [49]. Simply, by accurate control of the precursor and calcination temperature, we prepared series of electrocatalysts with bimetals (Co and W) embedded N-doping carbon-nanofibers (CNFs). Another highlight of this strategy is the products are self-supported which eliminates extra interference during the electrode treatment. The entire strategy for the construction of Co_6W_6C–N@CNFs is schematically illustrated in Fig. 1 The nanofiber membranes collected by electrospun were firstly dried at 60 °C in an oven for 12 h. After sequent peroxidation process, catalysts were heated in Ar atmosphere at 900 °C to obtain the Co_6W_6C–N@CNFs, which possesses superior HER catalytic activities and stability in both acidic and base solution with very low overpotentials of 85 and 116 mV at η_{10} and small Tafel slopes of 86 and 101 mV dec^{-1}, respectively.

Experimental methods

Chemicals and materials

Ammonium metatungstate hydrate ($(NH_4)_6H_2W_{12}O_{40}\cdot xH_2O$) was purchased from Sigma-Aldrich. Cobaltous nitrate

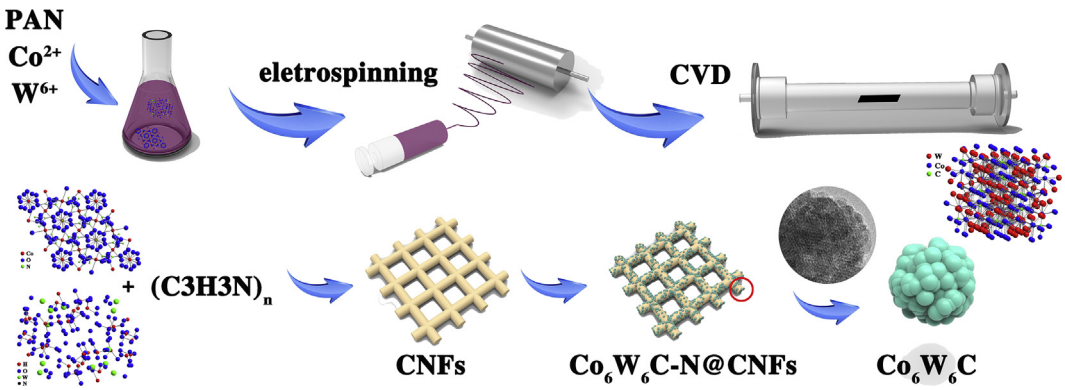

Fig. 1 – The schematic illustration of the Co_6W_6C–N@CNFs synthesis process.

($Co(NO_3)_2 \cdot 6H_2O$) was supplied by Shanghai Macklin Biochemical Co., Ltd. China. Dimethylformamide (DMF, 99.5%) were procured from Shanghai Civi Chemical Technology Co., Ltd. Sulfuric acid (H_2SO_4) and potassium hydroxide (KOH) were supplied by Aladdin Co., Ltd. Polyacrylonitrile (PAN, $M_w \approx 1.4 \times 10^5$, copolymerized with 10 wt % methyl acrylate) was purchased by Sinopec Shanghai Petrochemical Co., Ltd. Ultrapure water (Milli-Q) was used throughout the experiments. All the chemicals mentioned are analytical grade and employed as received without any purification.

Synthesis of stacked CoWC nanocrystals anchored on carbon nanofibers

All the samples were prepared according to typical synthesis process [50]. A total metal salt of 1.2 g with different mass ratio of Co/W (1/2, 1/1, 2/1) were firstly added into 12.5 g DMF dissolved with 1.5 g PAN, followed by stirring for 12 h until the solution turn to be homogeneous, after which the clear solution was transferred into a plastic inject connected to a high voltage power supply. The applied voltage was 12.5 kV, the needle-to-collector distance was 12 cm, and the flow rate of the solution was 0.5 mL h^{-1}. The electrospun nanofiber membranes were carefully detached from the home-built collector, and then dried entirely at 60 °C for 12 h. After this stage, membranes were firstly peroxided in the furnace at 230 °C for 1 h, and then the chemical vapor deposition (CVD) treatment was carried out in Ar flow at high temperatures, ranging from 700 °C to 1000 °C, with heating rate of 7 °C min^{-1} and maintained for 3 h.

Synthesis of CNFs

Firstly, 1.5 g PAN was dissolved in 12.5 g DMF, before stirring for 12 h until the solution clear and followed by being transferred into a same plastic inject with concordant condition of voltage, needle-to-collector distance and flow rate. The subsequent peroxidation and CVD process were also keep the parallel as the synthesis of CoWC–N@CNFs.

Materials characterization

Field emission scanning electron microscopy (FE-SEM) images were characterized using a JSM-6700F FE-SEM (JEOL, Japan) at an accelerating voltage of 3 kV. Transmission electron microscopy (TEM) images were taken using a JSM-2100 transmission electron microscope (JEOL, Japan) at an accelerating voltage of 200 kV. The high-angle annular dark field scanning transmission electron microscopy (HAADF-STEM) images and STEM-EDX mappings (Tecnai G2 F30S-Twin, Philips-FEI) were observed by a STEM (Tacnai G2 F30 S-Twin, Philips-FEI) at an acceleration voltage of 300 kV. X-ray diffraction (XRD) patterns were analyzed using a Bruker AXS D8 DISCOVER X-ray diffractometer with Cu K_α radiation ($\lambda = 1.5406$ Å) at a scanning rate of 5° min^{-1} in the 2θ range of 20–80°. X-ray photoelectron spectra (XPS) of the products were recorded using an X-ray photoelectron spectrometer (Kratos Axis Ultra DLD) with an Al (mono) K_α source (1486.6 eV). The Al K_α source was operated at 15 kV and 10 mA.

Electrode preparation

Traditionally, to prepare the working electrode, glassy carbon electrode (GCE, 3 mm diameter) was polished with 1.0, 0.3 and 0.05 μm alumina slurry, and thoroughly washed before surface modification. 3 mg commercial Pt/C (Johnson-Matthey, 20 wt %) was dispersed in 1 mL of 3/1 (volumetric ratio) water/isopropanol mixed solvent with 20 μL of Nafion solution (5 wt %) under ultra-sonication for 30 min until a homogeneous ink formed. The Nafion solution was used as a proton conducting binder to ensure good adhesion onto the electrode. Thereafter, 5 μL of catalyst ink was dropped onto a GC disk electrode using a micropipette, and then drying at room temperature (loading 212.3 μg cm^{-2}). Moreover, the as-prepared catalyst film was stored in a desiccator at room temperature before use.

Electrochemical measurements

The electrochemical measurements were performed on a CHI660E workstation (Shanghai Chenhua, Shanghai) in a standard three-electrode system. A modified GCE, a Pt wire and a saturated calomel electrode (SCE) were served as the working electrode, counter electrode and reference electrode in 0.5 M H_2SO_4 and 1 M KOH electrolytes, respectively. All the potentials were referenced to a reversible hydrogen electrode (RHE) by adding a value of ($0.244 + 0.0592 \times pH$) V. The catalyst was first subject to cyclic voltammetry (CV) scans between

0 and 1.20 V vs the RHE at a scan rate of 100 mV s^{-1} until a stable CV was obtained. Then, linear sweep voltammetry (LSV) polarization curves were performed at scan rate of 1 mV s^{-1} and all the polarization curves were iR-compensation. The accelerated stability test was performed by potential cycling between −0.2 and 0.8 V vs RHE in acidic and between −2.0 and −1.0 V vs RHE in base at a sweep rate of 100 mV s^{-1} for 1000 cycles. At the end of the cycles, the resulting electrodes were used for polarization curves at a scan rate of 1 mV s^{-1}. Additionally, the frequencies used to obtain the Electrochemical impedance spectroscopy (EIS) ranged from 100 kHz to 0.001 Hz, and the stability test of the Co_6W_6C–N@CNFs were also used a typical three electrode cell. The Co_6W_6C–N@CNFs membrane was tailored into a neat square (1 × 1 cm) and directly utilized as the working electrode, and the current-time response was monitored by chronoamperometric measurements in 0.5 M H_2SO_4 and 1 M KOH electrolyte for 22 h and 12 h respectively. The electrochemically active surface areas (ECSA) were estimated by electrochemical double layer capacitance (C_{dl}). The CVs were measured in a non-Faradaic region at different scan rates of 20, 40, 60, 80, 100, 120, 140, 160, 180 and 200 mV s^{-1}. By plotting the anodic and cathodic current densities difference ((j_{anodic} - $j_{cathodic}$)/2) against the scan rate, a linear relationship was fitting and the slope is equal to C_{dl}. All measurements were performed at room temperature.

Results and discussion

The structure and morphology of Co_6W_6C–N@CNFs were firstly characterized and the SEM images (Fig. 2a and b) reveal the nanoparticles loaded on the surface of nanofibers with highly density. TEM result (Fig. 2c and d) further demonstrates that numerous stacked Co_6W_6C nanocrystals disperse uniformly on CNFs, indicating abundant active sites for HER. HRTEM image in Fig. 2e presents that the diameter of Co_6W_6C nanocrystal is ~2–6 nm and well-defined lattice fringes of 0.220 and 0.294 nm, corresponding to the (440) and (511) facets of Co_6W_6C, respectively. Notably, distorted carbon layers are obviously observed around Co_6W_6C particles, triggered by catalytic graphitization behavior at high calcination temperature, which cannot only shorten the charge transport and then improve the conductivity but also provide protection with catalysts [51]. EDX element mappings (Fig. 2f) also illustrate the uniform dispersion of C, N, O, Co and W in Co_6W_6C–N@CNFs. These results all manifest the homogeneously loaded Co_6W_6C–N on carbon nanofibers.

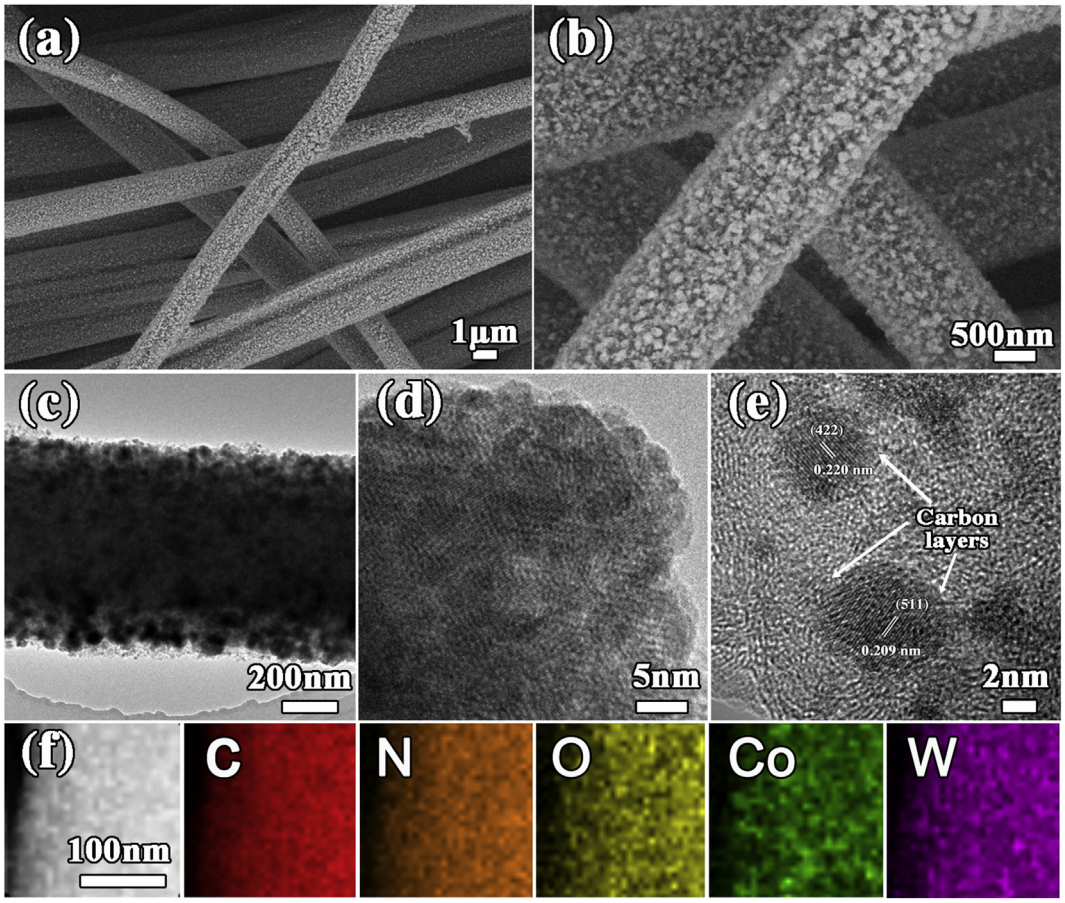

Fig. 2 – (a,b) SEM images of Co_6W_6C–N@CNFs with a low (a) and high (b) resolution, (c–e) TEM images of Co_6W_6C–N@CNFs: (c) Low-resolution, (d) HRTEM images of stacked Co_6W_6C nanocrystals, (e) HRTEM images of Co_6W_6C nanocrystal and (f) STEM-EDX elemental mapping of C, N, O, Co and W respectively.

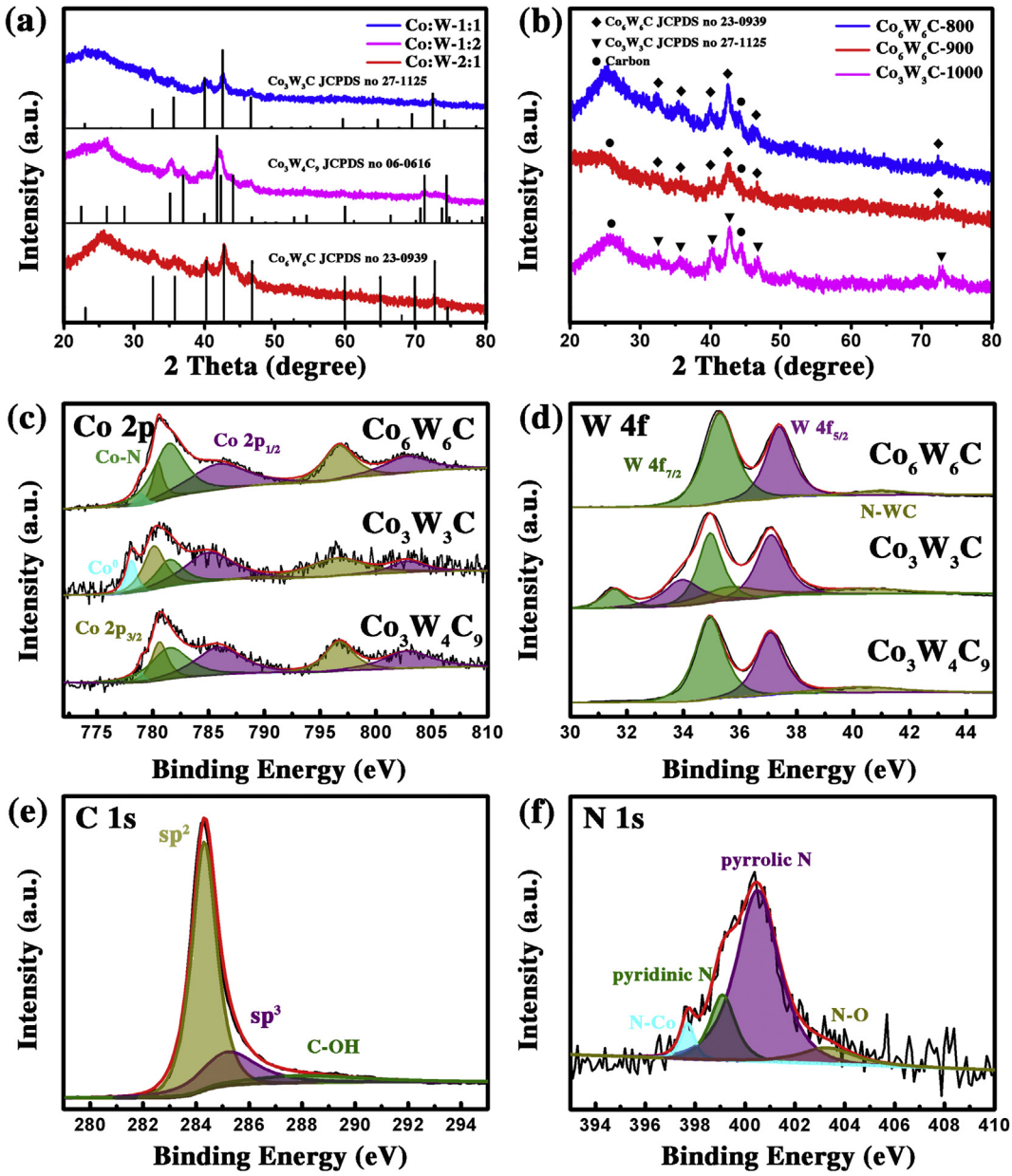

Fig. 3 – (a) XRD patterns of Co_3W_3C–N@CNFs, Co_6W_6C–N@CNFs and $Co_3W_4C_9$–N@CNFs, (b) XRD patterns of Co_6W_6C-800, Co_6W_6C-900 and Co_3W_3C-1000, (c–d) XPS spectra of Co_3W_3C–N@CNFs, Co_6W_6C–N@CNFs and $Co_3W_4C_9$–N@CNFs. Peaking fitting of (c) Co 2s, (d) W 4f, (e–f) XPS spectra of Co_6W_6C–N@CNFs. Peaking fitting of (e) C 1s and (f) N 1s.

Fig. 3a and b describe the X-ray diffraction (XRD) patterns of all samples prepared in this work, with unequal ratios of metal salt (Fig. 3a) and different carbonization temperatures (Fig. 3b). Fig. 3a reveals that three different compounds formed depending on series of Co/W ratio. When the ratio came to 2/1, Co_6W_6C was produced, fitted with the standard card of JCPDS 23–0939; When it came to 1/1, Co_3W_3C was prepared (Fig. S1), which is confirmed by the standard card of JCPDS 27–1125; When the mass of W doubled to the Co, $Co_3W_4C_9$ was formed, as shown in Fig. S2. The influence of carbonization temperature for crystal formation can be presented in Fig. 3b that demonstrates the crystal transformation and the crystal size are closed related to high temperature. The broad peaks around 26° and 45° were characteristic peaks of carbon from matrix, the other peaks were fitted well with Co_3W_3C and Co_6W_6C. Compared to the morphology of Co_6W_6C-800, Figs. S3 and S4 manifest that the crystal size shrank from 30 nm to 5 nm with the temperature rising from 700 °C to 900 °C, which benefits catalytic property by increasing the number and the specific surface area of active sites. Notably, when temperature increased, Co_6W_6C crystals transferred to Co_3W_3C phase (which is also named as $Co_6W_6C_2$ (Fig. S5)) [52], and in this work, XRD patterns of samples show a slightly positive shift from 900 °C to 1000 °C.

Further electronic structure analysis in Fig. 3c and d present the high-resolution spectra of Co 2p and W 4f of three samples, respectively. It is worth note that in Fig. 3c, all the samples showed four obvious peaks of Co $2p_{3/2}$, Co $2p_{1/2}$ and

their shakeup satellites. In comparison to the XPS peak centered at 781.1 eV corresponding to standard Co $2p_{3/2}$ [53], here are negative shifts of Co_6W_6C ($\Delta E = 0.6$ eV) and $Co_3W_4C_9$ ($\Delta E = 0.5$ eV) inferring the electron transportation from donor Co to W and N, which is also confirmed by a 0.3 eV negative shift of the corresponding peak of Co $2p_{1/2}$ in Co_3W_3C. And it can also verify the stronger electronic interaction between Co and W in Co_6W_6C than that in others. In addition, the peaks at 779 eV (Co_6W_6C and $Co_3W_4C_9$) and 778.7 eV (Co_3W_3C) are attributed to metallic Co (Co^0) [54,55], and peaks at 781.5 eV are ascribed to Co–N bonding, which is manifested straightforwardly the coupling effect between Co and N elements [56].

Fig. 3d compares the spectra of W 4f from samples, in which Co_6W_6C and $Co_3W_4C_9$ show the same patterns of two apparent characteristic peaks of W $4f_{7/2}$ (34.9 eV) and W $4f_{5/2}$ (37 eV) [57], with a 0.2 eV positive shift of W $4f_{7/2}$ in Co_6W_6C. A relatively strong peak at 41 eV in Co_6W_6C is attributed to the oxidation of N-WC [58], while the remaining peak at 40.3 eV in $Co_3W_4C_9$ is assigned to W–C [59], which can also be observed in Co_3W_3C. However, the chemical environment of W 4f in Co_3W_3C is more complex with four peaks appearing at 31.7 eV, 33.9 eV, 35.6 eV and 37.7 eV corresponded to W $4f_{7/2}$, W $4f_{5/2}$ and their satellite structures, respectively [53]. Additionally, because of the inevitable oxidation in the surface [57], here is a peak at 34.9 eV represents the existence of WO_3. Furthermore, Fig. 3e and f reveal the high-resolution XPS of C 1s and N 1s of Co_6W_6C–N@CNFs. Fig. 3e describes the major bonding energy of C is originating from the graphene-like sp^2, sp^3 carbon and C–OH [53]. The main peaks in Fig. 3f are ascribed to pyrrolic and pyridinic N that reported as promoting substances for HER [60]. Other peaks at 397.7 eV and 403.3 eV are corresponded to N–Co and N–O, respectively [61], further confirming the coupling interaction between Co and N, while the N–O is attributed to the oxidation of matrix, as shown in Fig. S5.

The HER catalytic performance of Co_6W_6C–N@CNFs was firstly accessed by LSV in acidic medium (0.5 M H_2SO_4, pH ≈ 0). The polarization curves with 95% iR-correction are shown in Fig. 4a The 20 wt % Pt/C catalyst delivers the best HER catalytic activity. A tiny overpotential of 85 mV at η_{10}, only 50 mV larger than that for Pt/C, was required for Co_6W_6C–N@CNFs, indicating its outstanding HER electrocatalytic performance. In terms of the overpotential of η_{10}, $Co_3W_4C_9$–N@CNFs and Co_3W_3C–N@CNFs exhibit sluggish catalytic activities with overpotentials of 222 and 204 mV, respectively. The corresponding Tafel slope of Co_6W_6C–N@CNFs is 85 mV dec^{-1} in 0.5 M H_2SO_4 (Fig. 4b), also lower than that of Co_3W_3C–N@CNFs (173 mV dec^{-1}) and $Co_3W_4C_9$–N@CNFs (197 mV dec^{-1}), which indicates the most efficient reaction kinetics upon Co_6W_6C–N@CNFs hybrids to undergo a rapid hydrogen production. The value of 85 mV dec^{-1} manifests a Volmer-Heyrovsky mechanism [62], where the Heyrovsky reaction is considered as the main time-controlling step and the Volmer reaction of H^+ to H_{abs} is much faster [63]. Thus, the accelerated kinetics could be ascribed to promote the Volmer process, paving a direct and smooth pathway for subsequent reactions [24]. Meanwhile, we also investigated their electrocatalytic performance in base environment. As shown in Fig. 4c and d, Co_6W_6C–N@CNFs possesses the superior HER activity among as-prepared samples, with overpotential of 116 mV at η_{10} and Tafel slope of 101 mV dec^{-1}. These results reveal the parallel favorable reaction kinetics of Co_6W_6C–N@CNFs in base media, albeit hydrone has to decompose in advance due to a lower H^+ environment, where the HER mechanism turns to: (1) $H_2O + e^- + * \rightarrow H_{abs} + OH^-$ (Volmer reaction); (2) $H_{abs} + H_2O + e^- \rightarrow H_2 + OH^- + *$ (Heyrovsky reaction) [64].

Moreover, we also evaluated the impact of carbonization temperature to HER activity in acidic and alkali solution. With the rise of carbonization temperature, the overpotentials at η_{10} increased firstly from 246 mV at 800 °C, reaching to the best performance at 900 °C (86 mV), and then dropped to 204 mV at 1000 °C in acidic solution (Fig. 4e). The Tafel slope values show the parallel result of 229 and 115 mV dec^{-1} attributed to 800 °C and 1000 °C, respectively, which are both larger than that of 900 °C (85 mV dec^{-1}), manifesting that 900 °C is the optimal temperature for catalytically active Co_6W_6C crystal growth. Then we carried out the further investigation of HER kinetics in alkali environment. Likewise, the electrocatalytic properties of HER in base environment show a similar pattern in Fig. S6, with overpotential of 182 mV, 168 mV and 116 mV required for 800 °C, 900 °C and 1000 °C samples, respectively. Perhaps the crystal transformation and crystal growth influence the number and exposure of active sites, thus make a difference on catalytic property, which conduces to the corresponding Tafel slope of Co_6W_6C-900 in 1.0 M KOH (Fig. 4f) is 101 mV dec^{-1}, lower than that of 177 and 185 mV dec^{-1} for Co_3W_3C-1000 and Co_6W_6C-800, respectively, suggesting the faster kinetics for sample produced at 900 °C.

EIS tests were also applied to examine the interface characteristics and electrochemical kinetics of Co_6W_6C–N@CNFs. Nyquist plots in Fig. 5a were fitted by the equivalent circuit, which consists of two pathways: CPE1-R_{ct} for charge-transfer and CPE2-R_p for surface porosity, and the R_c and R_s represent the contact resistance among catalyst layers and the solution resistance, respectively [54]. This result reveals that at open-circuit voltage, the R_{ct} values for Co_6W_6C–N@CNFs, Co_3W_3C–N@CNFs and $Co_3W_4C_9$–N@CNFs in acidic solution are 5.0, 8.2 and 13.8 Ω, respectively, indicating the resistances of electron transfer and mass transport upon Co_6W_6C–N@CNFs are lower than others. Compared to Fig. S10, the R_{ct} values in base environment is much larger than those in acidic solution (5.8 Ω for Co_6W_6C–N@CNFs, 8.4 Ω for Co_3W_3C–N@CNFs and 13.8 Ω for $Co_3W_4C_9$–N@CNFs), showing the slower HER reaction kinetics that caused by an additional hydrone decomposition step in base medium. Meanwhile, in pH ≈ 14, Co_6W_6C-1000 possesses lower resistance than Co_6W_6C-800, as shown in Fig. 5b, at 11.8 and 14 Ω, respectively. The parallel results were also presented in acidic condition in Fig. S10. Overall, it is worth mentioning that Co_6W_6C–N@CNFs exhibits the smallest R_{ct} among these catalysts both in acidic and base environment.

The double-layer capacitance (C_{dl}, Fig. 5c) of Co_6W_6C–N@CNFs in acidic solution gives a high value of 179.49 mF cm^{-2}, which is 42.3, 56.3, 75.2 and 131.1 mF cm^{-2} larger than that of Co_3W_3C-1000, Co_3W_3C–N@CNFs, $Co_3W_4C_9$–N@CNFs and Co_6W_6C-800, respectively. The Higher C_{dl}

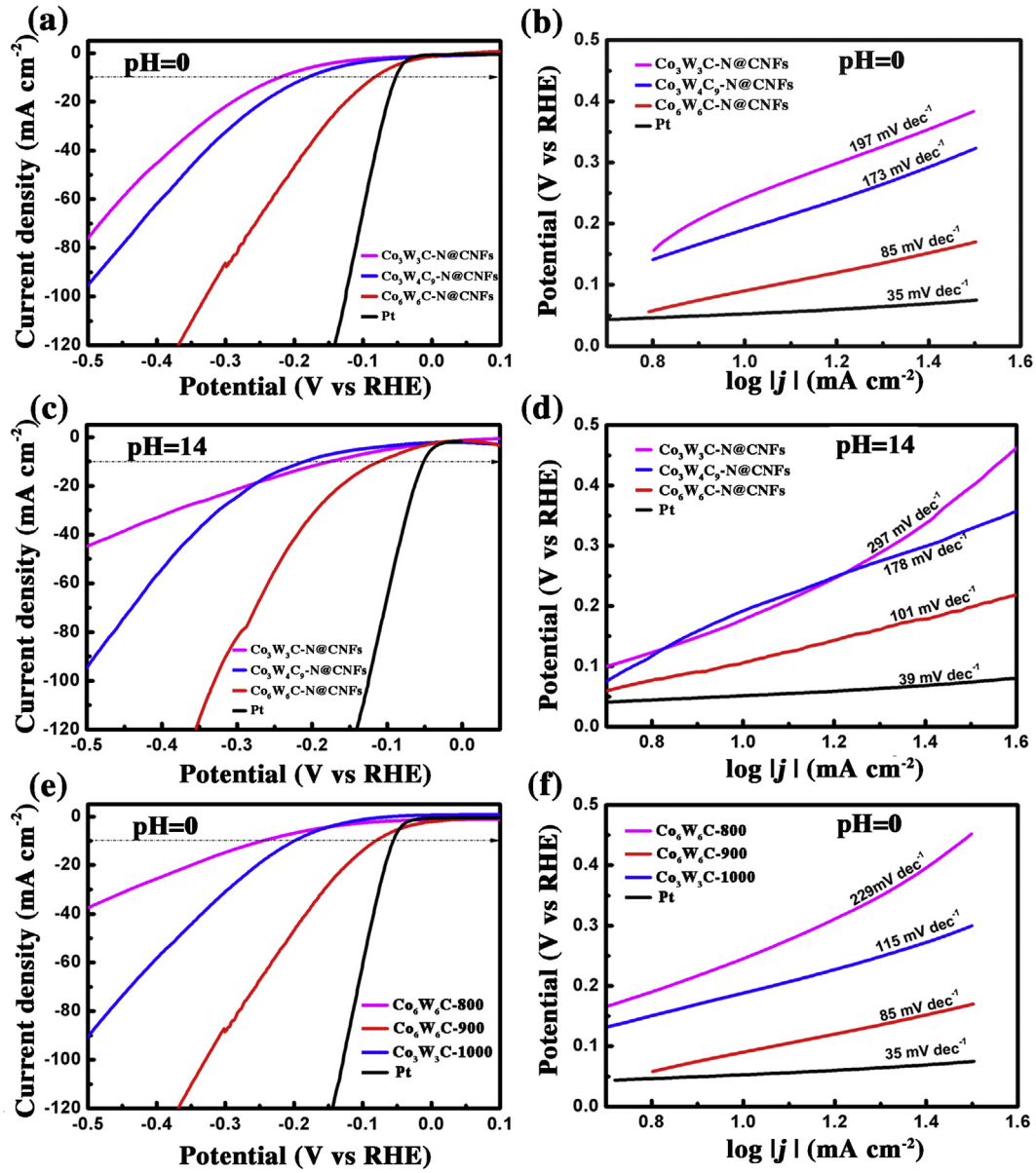

Fig. 4 – HER characteristics. (a, c, e) Polarization curves of HER: (a) Co_3W_3C–N@CNFs, Co_6W_6C–N@CNFs and $Co_3W_4C_9$–N@CNFs in 0.5 M H_2SO_4, (c) 1 M KOH, (e) Co_6W_6C-800, Co_6W_6C-900 and Co_3W_3C-1000 in 0.5 M H_2SO_4. The corresponding Tafel plots derived from the polarization curves (b, d, f): (b) Co_3W_3C–N@CNFs, Co_6W_6C–N@CNFs and $Co_3W_4C_9$–N@CNFs in 0.5 M H_2SO_4, (d) 1 M KOH, (f) Co_6W_6C-800, Co_6W_6C-900 and Co_3W_3C-1000 in 0.5 M H_2SO_4.

value indicates the larger electrochemical active surface area of Co_6W_6C–N@CNFs and also represent growing abundant active sites [65]. Similarly, the outcome in base solution was deduced in Fig. 5d, Co_6W_6C–N@CNFs at 143.1 mF cm^{-2}, Co_3W_3C-1000 at 79.4 mF cm^{-2}, Co_3W_3C–N@CNFs at 62.9 mF cm^{-2}, Co_6W_6C-800 at 51.9 mF cm^{-2} and $Co_3W_4C_9$–N@CNFs at the thinnest 34.5 mF cm^{-2}.

Another dimension of superb performance was reflected at robust durability. As shown in Fig. 5e and f, the catalytic activities could be maintained for at least 20 h and 12 h at η_{10} in acidic and base, respectively. And there is no obvious decay in the LSV curve after 1000 cycles of CV (insets of Fig. 5e and f) in both solution. After electrochemical test, we characterized the morphology of the material, showing in Figs. S13–S14. The Co_6W_6C–N particles of the catalysts remained relatively intact with slight drop in acidic, while in base condition, there are obvious impurities on the surface due to the oxidation of Co species [66].

Our work demonstrated the superb HER catalytic performances of the Co_6W_6C–N@CNFs catalyst, ascribed to its abundant active sites and the synergistically catalytic improvement of Co and W incorporated in N-doping carbon nanofibers. Importantly, the ultrathin nanocrystal size plays to the exposure of active sites. Moreover, the choice of matrix materials successively provides highly conductive network that enhances fast charge transport and stability in the both conditions, and carbon layers conduce to protect metal catalysts from agglomeration and corrosion during HER.

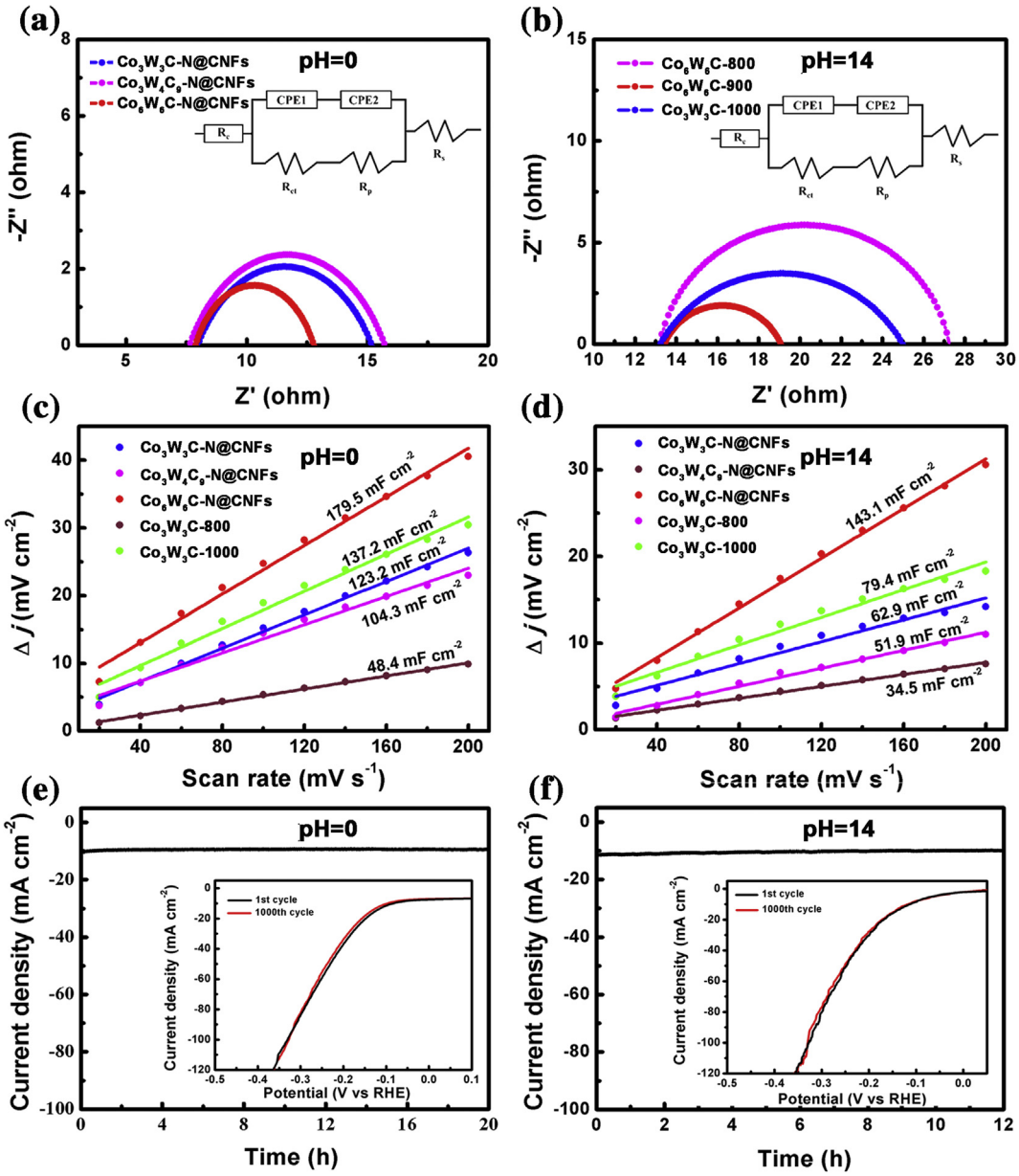

Fig. 5 – Electrochemical performance and HER stability: (a) Nyquist plots of Co_3W_3C–N@CNFs, Co_6W_6C–N@CNFs and $Co_3W_4C_9$–N@CNFs. (b) Co_6W_6C-800, Co_6W_6C-900 and Co_3W_3C-1000. (c) Capacitive current at 0.156 V as a function of scan rate of Co_3W_3C–N@CNFs, Co_6W_6C–N@CNFs and $Co_3W_4C_9$–N@CNFs (d) Co_6W_6C-800, Co_6W_6C-900 and Co_3W_3C-1000. (e) Chronopotentiometric curves at η_{10}; the inset in (e) is polarization curves of Co_6W_6C–N@CNFs before and after long-term electrolysis in 0.5 M H_2SO_4. (f) 1 M KOH.

Furthermore, the introduction of N atoms can not only optimize the adsorption energy of the surface, but also further promote the connection between the conductive substrate and the catalysts. Indeed, all these factors above cooperate synergistically to achieve optimal HER catalytic activities of the Co_6W_6C–N@CNFs.

Conclusion

In this investigation, stacked Co_6W_6C nanocrystals anchored on N-doping carbon nanofibers were assembled and exhibit exceedingly low overpotentials and small Tafel slopes in acidic (η_{10} = 86 mV, 85 mV dec^{-1}) and base (η_{10} = 116 mV, 101 mV dec^{-1}), with excellent stability. On the account of ultrathin nanocrystal sizes, Co_6W_6C–N@CNFs expose numerous active sites for HER. Due to the strong synergetic behavior between Co and W, and the modification of electronic structure by doping N atoms, which will optimize the adsorption energy of its surface, the Co_6W_6C–N@CNFs show excellent catalytic activities. Moreover, because of the existence and protection of carbon, it presents superb conductivity and durable stability.

Acknowledgments

This study was supported by the Natural Science Foundation of Zhejiang Province (Grant No. LQ16E020005).

Appendix A. Supplementary data

Supplementary data to this article can be found online at https://doi.org/10.1016/j.ijhydene.2019.11.123.

REFERENCES

[1] Kang HW, Lim SN, Song D, Park SB. Organic-inorganic composite of g-C_3N_4–$SrTiO_3$:Rh photocatalyst for improved H_2 evolution under visible light irradiation. Int J Hydrogen Energy 2012;37:11602–10.
[2] Lin L, Zhou W, Gao R, Yao S, Zhang X, Xu W, et al. Low-temperature hydrogen production from water and methanol using Pt/α-MoC catalysts. Nature 2017;544:80–3.
[3] Xia A, Cheng J, Song W, Su H, Ding L, Lin R, et al. Fermentative hydrogen production using algal biomass as feedstock. Renew Sustain Energy Rev 2015;51:209–30.
[4] Rodionova MV, Poudyal RS, Tiwari I, Voloshin RA, Zharmukhamedov SK, Nam HG, et al. Biofuel production: challenges and opportunities. Int J Hydrogen Energy 2017;42:8450–61.
[5] Winter CJ. Hydrogen energy — abundant, efficient, clean: a debate over the energy-system-of-change. Int J Hydrogen Energy 2009;34:S1–52.
[6] Bullock RM, Appel AM, Helm ML. Production of hydrogen by electrocatalysis: making the H–H bond by combining protons and hydrides. Chem Commun 2014;50:3125–43.
[7] Wang J, Cui W, Liu Q, Xing Z, Asiri AM, Sun X. Recent progress in cobalt-based heterogeneous catalysts for electrochemical water splitting. Adv Mater 2016;28:215–30.
[8] Heim LE, Schlörer NE, Choi JH, Prechtl MHG. Selective and mild hydrogen production using water and formaldehyde. Nat Commun 2014;5.
[9] Lei C, Wang Y, Hou Y, Liu P, Yang J, Zhang T, et al. Efficient alkaline hydrogen evolution on atomically dispersed Ni–N_x Species anchored porous carbon with embedded Ni nanoparticles by accelerating water dissociation kinetics. Energy Environ Sci 2019;12:149–56.
[10] Lu F, Zhou M, Zhou Y, Zeng X. First-row transition metal based catalysts for the oxygen evolution reaction under alkaline conditions: basic principles and recent advances. Small 2017;13.
[11] Xu Y, Li Y, Yin S, Yu H, Xue H, Li X, et al. Ultrathin nitrogen-doped graphitized carbon shell encapsulating CoRu bimetallic nanoparticles for enhanced electrocatalytic hydrogen evolution. Nanotechnology 2018;29:225403.
[12] Fu L, Hu X, Li Y, Cheng G, Luo W. IrW nanobranches as an advanced electrocatalyst for pH-universal overall water splitting. Nanoscale 2019;11:8898–905.
[13] Wen L, Sun Y, Zhang T, Bai Y, Li X, Lyu X, et al. $MnMoO_4$ nanosheet array: an efficient electrocatalyst for hydrogen evolution reaction with enhanced activity over a wide pH range. Nanotechnology 2018;29:335403.
[14] Shi J, Pu Z, Liu Q, Asiri AM, Hu J, Sun X. Tungsten nitride nanorods array grown on carbon cloth as an efficient hydrogen evolution cathode at all pH values. Electrochim Acta 2015;154:345–51.
[15] Xue Y, Li J, Xue Z, Li Y, Liu H, Li D, et al. Extraordinarily durable graphdiyne-supported electrocatalyst with high activity for hydrogen production at all values of pH. ACS Appl Mater Interfaces 2016;8:31083–91.
[16] Zhu Y, Chen G, Zhong Y, Zhou W, Liu M, Shao Z. An extremely active and durable Mo_2C/graphene-like carbon based electrocatalyst for hydrogen evolution reaction. Mater Today Energy 2017;6:230–7.
[17] Tao BX, Ye C, Li XL, Wang XH, Chen G, Li LJ, et al. Heterogeneous cobalt phosphides nanoparticles anchored on carbon cloth realizing the efficient hydrogen generation reaction. Int J Hydrogen Energy 2019;44:531–9.
[18] Gao W, Shi Y, Zhang Y, Zuo L, Lu H, Huang Y, et al. Molybdenum carbide anchored on graphene nanoribbons as highly efficient all-pH hydrogen evolution reaction electrocatalyst. ACS Sustainable Chem Eng 2016;4:6313–21.
[19] Chen X, Qi J, Wang P, Li C, Chen X, Liang C. Polyvinyl alcohol protected Mo_2C/Mo_2N multicomponent electrocatalysts with controlled morphology for hydrogen evolution reaction in acid and alkaline medium. Electrochim Acta 2018;273:239–47.
[20] Hu WH, Shang X, Xue J, Dong B, Chi JQ, Han GQ, et al. Activating MoS_2/CNs by tuning (001) plane as efficient electrocatalysts for hydrogen evolution reaction. Int J Hydrogen Energy 2017;42:2088–95.
[21] Lu XF, Yu L, Lou XW. Highly crystalline Ni-doped FeP/carbon hollow nanorods as all-pH efficient and durable hydrogen evolving electrocatalysts. Sci Adv 2019;5.
[22] Yang S, Wang Y, Zhang H, Zhang Y, Liu L, Fang L, et al. Unique three-dimensional $Mo_2C@MoS_2$ heterojunction nanostructure with S vacancies as outstanding all-pH range electrocatalyst for hydrogen evolution. J Catal 2019;371:20–6.
[23] Yu J, Li WJ, Zhang H, Zhou F, Li R, Xu CY, et al. Metallic $FePSe_3$ nanoparticles anchored on N-doped carbon framework for all-pH hydrogen evolution reaction. Nano Energy 2019;57:222–9.
[24] Zhang R, Wang X, Yu S, Wen T, Zhu X, Yang F, et al. Ternary $NiCo_2P_x$ nanowires as pH-universal electrocatalysts for highly efficient hydrogen evolution reaction. Adv Mater 2017;29.
[25] Li J, Liu G, Liu B, Min Z, Qian D, Jiang J, et al. An extremely facile route to Co_2P encased in N,P-codoped carbon layers: highly efficient bifunctional electrocatalysts for ORR and OER. Int J Hydrogen Energy 2018;43:1365–74.
[26] He C, Tao J. Two-dimensional TaC nanosheets on a reduced graphene oxide hybrid as an efficient and stable electrocatalyst for water splitting. Chem Commun 2016;52:8810–3.
[27] Chen WF, Schneider JM, Sasaki K, Wang CH, Schneider J, Iyer S, et al. Tungsten carbide-nitride on graphene nanoplatelets as a durable hydrogen evolution electrocatalyst. Chemsuschem 2014;7:2414–8.
[28] Gong Q, Wang Y, Hu Q, Zhou J, Feng R, Duchesne PN, et al. Ultrasmall and phase-pure W_2C nanoparticles for efficient electrocatalytic and photoelectrochemical hydrogen evolution. Nat Commun 2016;7:13216.
[29] Yang Q, He Y, Fan Y, Chen X, Li Y. Efficient hydrogen evolution electrocatalysts from Li_xMoS_2 nanoparticles on three-dimensional substrate. Int J Hydrogen Energy 2017;42:6482–9.
[30] Liu Y, Yu G, Li GD, Sun Y, Asefa T, Chen W, et al. Coupling Mo_2C with nitrogen-rich nanocarbon leads to efficient hydrogen-evolution electrocatalytic sites. Angew Chem Int Ed Engl 2015;54:10752–7.
[31] Cheng R, He H, Pu Z, Amiinu IS, Chen L, Wang Z, et al. Shrunken hollow Mo-N/Mo-C nanosphere structure for efficient hydrogen evolution in a broad pH range. Electrochim Acta 2019;298:799–805.

[32] Yang S, Xie M, Chen L, Wei W, Lv X, Xu Y, et al. Cobalt phosphide nanoparticles embedded in 3D N-doped porous carbon for efficient hydrogen and oxygen evolution reactions. Int J Hydrogen Energy 2019;44:4543–52.
[33] Chen Z, Jia H, Yuan J, Liu X, Fang C, Fan Y, et al. P-co-doped carbon coupled with CoP as superior electrocatalysts for hydrogen evolution reaction and overall water splitting. Int J Hydrogen Energy 2019;44:24342–52.
[34] Park N, Hong S, Kim G, Jhi SH. Computational study of hydrogen storage characteristics of covalent-bonded graphenes. J Am Chem Soc 2007;129:8999–9003.
[35] Zhang C, Fu L, Liu N, Liu M, Wang Y, Liu Z. Synthesis of nitrogen-doped graphene using embedded carbon and nitrogen sources. Adv Mater 2011;23:1020–4.
[36] Kuang M, Wang Q, Han P, Zheng G. Cu, Co-embedded N-enriched mesoporous carbon for efficient oxygen reduction and hydrogen evolution reactions. Adv Energy Mater 2017;7.
[37] Cao GX, Xu N, Chen ZJ, Kang Q, Dai HB, Wang P. Cobalt-tungsten-boron as an active electrocatalyst for water electrolysis. Chem Select 2017;2:6187–93.
[38] Liu Y, Li GD, Yuan L, Ge L, Ding H, Wang D, et al. Carbon-protected bimetallic carbide nanoparticles for a highly efficient alkaline hydrogen evolution reaction. Nanoscale 2015;7:3130–6.
[39] Zou X, Zhang Y. Noble metal-free hydrogen evolution catalysts for water splitting. Chem Soc Rev 2015;44:5148–80.
[40] Liu Y, Li Q, Si R, Li GD, Li W, Liu DP, et al. Coupling sub-nanometric copper clusters with quasi-amorphous cobalt sulfide yields efficient and robust electrocatalysts for water splitting reaction. Adv Mater 2017;29.
[41] You B, Jiang N, Sheng M, Gul S, Yano J, Sun Y. High-performance overall water splitting electrocatalysts derived from cobalt-based metal–organic frameworks. Chem Mater 2015;27:7636–42.
[42] Zeng M, Chen Y, Li J, Xue H, Mendes RG, Liu J, et al. 2D WC single crystal embedded in graphene for enhancing hydrogen evolution reaction. Nano Energy 2017;33:356–62.
[43] Sun T, Wu Q, Che R, Bu Y, Jiang Y, Li Y, et al. Alloyed Co–Mo nitride as high-performance electrocatalyst for oxygen reduction in acidic medium. ACS Catal 2015;5:1857–62.
[44] Song LJ, Meng HM. Effect of carbon content on Ni–Fe–C electrodes for hydrogen evolution reaction in seawater. Int J Hydrogen Energy 2010;35:10060–6.
[45] Wang F, Sun Y, He Y, Liu L, Xu J, Zhao X, et al. Highly efficient and durable MoNiNC catalyst for hydrogen evolution reaction. Nano Energy 2017;37:1–6.
[46] Han N, Yang KR, Lu Z, Li Y, Xu W, Gao T, et al. Nitrogen-doped tungsten carbide nanoarray as an efficient bifunctional electrocatalyst for water splitting in acid. Nat Commun 2018;9:924.
[47] Yang J, Xie Y, Wang R, Jiang B, Tian C, Mu G, et al. Synergistic effect of tungsten carbide and palladium on graphene for promoted ethanol electrooxidation. ACS Appl Mater Interfaces 2013;5:6571–9.
[48] Ma R, Zhou Y, Chen Y, Li P, Liu Q, Wang J. Ultrafine molybdenum carbide nanoparticles composited with carbon as a highly active hydrogen-evolution electrocatalyst. Angew Chem Int Ed 2015;54:14723–7.
[49] Wen Y, Zhu H, Zhang L, Zhang S, Zhang M, Du M. Activating MoS_2 by interface engineering for efficient hydrogen evolution catalysis. Mater Res Bull 2019;112:46–52.
[50] Zhu H, Gu L, Yu D, Sun Y, Wan M, Zhang M, et al. The marriage and integration of nanostructures with different dimensions for synergistic electrocatalysis. Energy Environ Sci 2017;10:321–30.
[51] Wen Y, Zhu H, Zhang L, Hao J, Wang C, Zhang S, et al. Beyond colloidal synthesis: nanofiber reactor to design self-supported core–shell $Pd_{16}S_7/MoS_2$/CNFs electrode for efficient and durable hydrogen evolution catalysis. ACS Appl Energy Mater 2019;2:2013–21.
[52] Vesel A, Mozetic M, Balat-Pichelin M. Phase transformation in tungsten carbide–cobalt composite during high temperature treatment in microwave hydrogen plasma. Ceram Int 2012;38:6107–13.
[53] He C, Tao J. Two-dimensional Co_3W_3C nanosheets on graphene nanocomposition: an Pt-like electrocatalyst toward hydrogen evolution reaction in wide pH range. Mater Today Energy 2018;8:65–72.
[54] He C, Tao J. Three-dimensional hollow porous Co_6Mo_6C nanoframe as an highly active and durable electrocatalyst for water splitting. J Catal 2017;347:63–71.
[55] He C, Zhang S, Tao J, Qiu Y. Ultrafine Co_6Mo_6C nanocrystals on reduced graphene oxide as efficient and highly stable electrocatalyst for hydrogen generation. Int J Hydrogen Energy 2018;43:20323–31.
[56] Feng X, Bo X, Guo L. CoM(M=Fe,Cu,Ni)-embedded nitrogen-enriched porous carbon framework for efficient oxygen and hydrogen evolution reactions. J Power Sources 2018;389:249–59.
[57] Zeng J, Yanglee J. Ruthenium-free, carbon-supported cobalt and tungsten containing binary & ternary Pt catalysts for the anodes of direct methanol fuel cells. Int J Hydrogen Energy 2007;32:4389–96.
[58] He Y, Wang L, Jia D, Zhao Z, Qiu J. $NiWO_4$/Ni/Carbon composite fibres for supercapacitors with excellent cycling performance. Electrochim Acta 2016;222:446–54.
[59] Alhajri NS, Anjum DH, Takanabe K. Molybdenum carbide-carbon nanocomposites synthesized from a reactive template for electrochemical hydrogen evolution. J Mater Chem 2014;2:10548–56.
[60] Pan Y, Sun K, Liu S, Cao X, Wu K, Cheong WC, et al. Core-shell ZIF-8@ZIF-67-derived CoP nanoparticle-embedded N-doped carbon nanotube hollow polyhedron for efficient overall water splitting. J Am Chem Soc 2018;140:2610–8.
[61] Feng X, Wang H, Bo X, Guo L. Bimetal–Organic framework-derived porous rodlike cobalt/nickel nitride for all-pH value electrochemical hydrogen evolution. ACS Appl Mater Interfaces 2019;11:8018–24.
[62] Morales-Guio CG, Stern LA, Hu X. Nanostructured hydrotreating catalysts for electrochemical hydrogen evolution. Chem Soc Rev 2014;43:6555–69.
[63] Jin H, Wang J, Su D, Wei Z, Pang Z, Wang Y. In situ cobalt-cobalt oxide/N-doped carbon hybrids as superior bifunctional electrocatalysts for hydrogen and oxygen evolution. J Am Chem Soc 2015;137:2688–94.
[64] Liu X, Dong C, Dong W, Wang X, Yuan X, Huang F. Co nanoparticles embedded in a 3D CoO matrix for electrocatalytic hydrogen evolution. RSC Adv 2016;6:38515–20.
[65] Anantharaj S, Ede SR, Karthick K, Sam Sankar S, Sangeetha K, Karthik PE, et al. Precision and correctness in the evaluation of electrocatalytic water splitting: revisiting activity parameters with a critical assessment. Energy Environ Sci 2018;11:744–71.
[66] Liu YC, Koza JA, Switzer JA. Conversion of electrodeposited $Co(OH)_2$ to CoOOH and Co_3O_4, and comparison of their catalytic activity for the oxygen evolution reaction. Electrochim Acta 2014;140:359–65.